3 The CosmoGrid Simulation: Statistical Properties of Small Dark Matter Halos

Based on:
Tomoaki Ishiyama, Steven Rieder, Junichiro Makino, Simon Portegies Zwart, Derek Groen, Keigo Nitadori, Cees de Laat, Stephen McMillan, Kei Hiraki and Stefan Harfst
The Cosmogrid Simulation: Statistical Properties of Small Dark Matter Halos
Published in ApJ

We present the results of the ``CosmoGrid'' cosmological N-body simulation suites based on the concordance Lambda Cold Dark Matter (ΛCDM) model. The CosmoGrid simulation was performed in a 30Mpc box with 2048^3 particles. The mass of each particle is $1.28 \times 10^5 M_\odot$, which is sufficient to resolve ultra-faint dwarfs. We found that the halo mass function shows good agreement with the Sheth and Tormen (1999) fitting function down to $\sim 10^7 M_\odot$. We have analysed the spherically averaged density profiles of the three most massive haloes which are of galaxy group size and contain at least 170 million particles.

The slopes of these density profiles become shallower than -1 at the inner most radius. We also find a clear correlation of halo concentration with mass. The mass dependence of the concentration parameter cannot be expressed by a single power law, however a simple model based on the Press-Schechter theory proposed by Navarro, Frenk, and White (1997) gives reasonable agreement with this dependence. The spin parameter does not show a correlation with the halo mass. The probability distribution functions for both concentration and spin are well fitted by the log-normal distribution for haloes with the masses larger than $\sim 10^8 M_\odot$. The subhalo abundance depends on the halo mass. Galaxy-sized haloes have 50% more subhaloes than $\sim 10^{11} M_\odot$ haloes have.

3.1 Introduction

According to the present standard ΛCDM model, the universe is thought to be composed primarily of Cold Dark Matter (CDM) and dark energy (White and Rees 1978; Peacock 1999). Structure formation of the universe proceeds hierarchically in this model. Smaller-scale structures collapse first, and then merge into larger-scale structures.

There is serious discrepancy between the distribution of subhaloes in galaxy-sized haloes obtained by numerical simulations and the observed number of dwarf galaxies in the Local Group (Klypin et al. 1999; Moore et al. 1999a). This ``missing dwarf problem'' is still considered to be one of the most serious problems in the CDM paradigm (e.g., Kroupa et al. 2010). In order to understand the origin of this discrepancy, it is necessary to perform high-resolution cosmological N-body simulations and obtain unbiased sample of galaxy-sized haloes with resolution high enough to obtain reliable statistics of subhaloes since the subhalo abundance shows large halo-to-halo variations (Ishiyama et al. 2009a).

Cosmological N-body simulations have been widely used to study the non-linear structure formation of the universe and have been an important tool for a better understanding of our universe. In order to study the spatial correlation of galaxies, the first cosmological N-body simulations were performed in the 1970s using approximately 1000 particles (e.g., Miyoshi and Kihara 1975; Fall 1978; Aarseth et al. 1979; Efstathiou 1979). Since then, the development of better simulation algorithms and improvements in the performance of computers allow us to use much larger numbers of particles and have drastically increased the resolution of cosmological simulations.

Today, it is not uncommon that the number of particles exceeds 10^9 in high-resolution simulations. In these works, the size of the simulation volumes is typically $[O(\mathrm{Gpc})]^3$ and populations of galaxy clusters, gravitational lensing, and the baryon acoustic oscillation are studied (e.g., Evrard et al. 2002; Wambsganss et al. 2004; Teyssier et al. 2009; Kim et al. 2009; Crocce et al. 2010). The simulation results are also used to construct mock halo catalogues for next generation large volume surveys. Others use simulations of $[O(100\mathrm{Mpc})]^3$ volumes to study the internal properties of galaxy-sized dark matter haloes, their formation, evolution, and statistical properties (e.g., Springel et al. 2005; Klypin et al. 2011; White et al. 2010).

Using the results of high-resolution simulations of small-scale structures, we can study the fine structures of galactic haloes, the distribution of subhaloes, their structures, and their dependence on the nature of dark matter. This information has a strong impact on the indirect search for dark matter since gamma-ray flux

by self-annihilation is proportional to local density if we consider neutralino as the candidate of dark matter. Thus, we can restrict the nature of dark matter using the results of high-resolution simulations of small-scale structures and indirect searches of dark matter. In addition, galaxies are considered to form in dark matter haloes with a mass larger than a critical value (Strigari et al. 2008; Li et al. 2009; Macciò et al. 2009; Okamoto and Frenk 2009). The structure of the smallest haloes which can host galaxies is important for the understanding of the galaxy formation processes.

The simulation of smaller-scale structures of dark matter haloes is not a trivial task since a very wide dynamic range of space, mass, and time must be covered. In particular, the number of time steps of such simulations is significantly larger than that of larger-scale simulations since the dynamical time-scale is proportional to $1.0/\sqrt{G\bar{\rho}}$, where $\bar{\rho}$ is the local density. Structures of smaller scales form earlier, and thus have higher densities, therefore, simulations of smaller scales are computationally more expensive.

Recently, simulations with galactic haloes of very high-resolution have been performed (Diemand et al. 2008; Springel et al. 2008; Stadel et al. 2009). These works used the re-simulation method, where one selects one or a few haloes at $z = 0$ from a simulation which covers a large volume (typically a cube of size O(100Mpc)) with a relatively low-resolution. The corresponding regions of these haloes are then identified in the initial particle distribution, and the particles in these regions are replaced by a larger number of smaller particles. After this is done, the entire volume is simulated to $z = 0$ again.

With this re-simulation method, we can resolve the structures of selected haloes with extremely high resolution (Diemand et al. 2008; Springel et al. 2008; Stadel et al. 2009). However, this method cannot be used for the study of halo-to-halo variations. Different haloes are born in different environments and grow differently. The difference in the environment and growth history must be the cause of halo-to-halo variations. Therefore, in order to study variations, we need a bias-free set of a large number of haloes. Clearly one cannot obtain a large number of haloes with re-simulation method in practical time.

In principle, one can improve the statistics by increasing the number of haloes selected for re-simulations. In order to avoid the selection bias, we need to apply random, bias-free selection, and the most reliable bias-free selection is to select all haloes, in other words, to simulate the entire simulation box with uniformly high mass resolution. Ishiyama et al. (2009a) performed the first bias-free high resolution simulation of small-scale structures. They analysed the statistics of the subhalo abundance using the complete set of haloes in the simulation box. The number of particles was 1600^3 in a 46.5Mpc cubic box and the mass of a particle was $10^6 M_\odot$.

The subhalo abundance showed large halo-to-halo variations (see also Ishiyama et al. 2008; Boylan-Kolchin et al. 2010). The concentration parameter and the radius at the moment of the maximum expansion showed fairly a tight correlation with the subhalo abundance. Halos formed earlier have a smaller number of subhaloes at present. This correlation suggests that the difference in the formation history is the origin of the variation of the subhalo abundance (see also Gao et al. 2004; van den Bosch et al. 2005; Zentner et al. 2005).

The Millennium-II simulation (Boylan-Kolchin et al. 2009) used a 137Mpc cubic box and the particle mass of $\sim 9.45 \times 10^6 M_\odot$. Its result is suitable for the analysis of the statistics of galaxy-sized dark matter haloes, because the number of haloes is larger than that of Ishiyama et al. (2009a). However, due to the lack of the mass resolution, it cannot be used to study the statistics of dwarf-galaxy-sized haloes and the statistics of subhaloes with the size larger than faint dwarf galaxy.

In this paper, we describe the first result of our CosmoGrid simulation. We simulated the evolution of haloes in a 30Mpc cubic box using 2048^3 particles. The mass of one particle is $1.28 \times 10^5 M_\odot$. The resolution reaches down to ultra-faint dwarf-galaxy-sized haloes ($\sim 10^7 M_\odot$) and is more than eight times better than that of our previous simulation (Ishiyama et al. 2009a). We focus on the halo mass function with the mass down to $10^7 M_\odot$, the structures of most massive haloes, and statistics of the internal properties of dwarf-galaxy-sized haloes. We describe our initial conditions and numerical settings in Section 3.2, and results in Section 3.3. We discuss and summarize our results in Section 3.4.

3.2 Initial Conditions and Numerical Method

The cosmological parameters adopted are based on the concordance ΛCDM cosmological model ($\Omega_0 = 0.3$, $\Omega_\Lambda = 0.7$, $h = 0.7$, $\sigma_8 = 0.8$, $n = 1.0$). These values are the same as those used in our previous simulation (Ishiyama et al. 2009a). We used a periodic cube of the co-moving size of 30Mpc. The number of particles for the largest run is 2048^3 which corresponds to a mass resolution of $1.28 \times 10^5 M_\odot$. To generate the initial particle distributions, we used the MPGRAFIC package (Prunet et al. 2008), which is a parallelised variation of the GRAFIC package (Bertschinger 2001). The initial redshift was 65.

In order to investigate the effect of the mass and spatial resolution, we performed two simulations with lower resolution. We generated the initial conditions for these low-resolution runs (CG1024 and CG512) by replacing 8 or 64 particles in the high-resolution initial condition (CG2048) with a single particle 8 or 64 times more massive. We did not use any smoothing filter for density and velocity spaces. The massive particles were picked up at regular intervals before perform-

Table 3.1: Run Parameters. Here, N, L, ε, and m are the total number of particles, the box length, the softening length, the mass resolution.

Name	N	L(Mpc)	ε(pc)	$m(\mathrm{M}_\odot)$
CG2048	2048^3	30.0	175	1.28×10^5
CG1024	1024^3	30.0	350	1.03×10^6
CG512	512^3	30.0	700	8.21×10^6
IFM2009 (Ishiyama et al. 2009a)	1600^3	46.5	700	1.00×10^6

Table 3.2: Global Parameters of Three Most Massive Group Sized Halos at $z = 0$. Here, M, N, $R_{\rm vir}$, $R_{\rm vmax}$, and $V_{\rm max}$ are the mass, the number of particles, the virial radius in which the spherical overdensity is 101 times the critical value, the radius where the rotation velocity is maximum, and the maximum rotation velocity, respectively.

Name	Run	$M(10^{13}M_\odot)$	N	$R_{\rm vir}$(kpc)	$R_{\rm vmax}$(kpc)	$V_{\rm max}$(kms^{-1})
GP1	CG2048	5.24	408499843	969	200	596
	CG1024	5.19	50632942	966	186	589
	CG512	5.22	6361253	968	184	596
GP2	CG2048	3.58	279382586	854	305	476
	CG1024	3.57	34836692	853	279	472
	CG512	3.57	4347651	852	294	475
GP3	CG2048	2.25	175752770	731	178	434
	CG1024	2.26	22072073	732	187	431
	CG512	2.25	2746874	731	192	434

ing the Zel'dovich approximation. This procedure introduces some aliasing noise in the high frequency limit of CG1024 and CG512 runs. The corresponding halo contains less than a few hundred particles. However, here we use CG1024 and CG512 runs for only convergence studies, and analyse haloes with the particles larger than ~ 1000. Thus, the effect of the aliasing noise should be negligible. In Table 3.1, we summarize parameters used in our simulations.

We used a leapfrog integrator with shared and adaptive time steps. The step size was determined as $\min(2.0\sqrt{\varepsilon/|\vec{a}_i|}, 2.0\varepsilon/|\vec{v}_i|)$ (minimum of these two values for all particles). All particles have the same time-steps. The gravitational Plummer softening length ε was 175pc at $z = 0$. The softening was constant in co-moving coordinates from $z = 65$ (initial condition) to $z = 10$. From $z = 10$ to $z = 0$, it was constant in physical coordinates. This procedure is similar to that used in Kawai et al. (2004).

For the largest simulation, we used four supercomputers. Three of them are Cray XT4 machines at the Center for Computational Astrophysics of National Astronomical Observatory of Japan, the Edinburgh Parallel Computing Centre in Edinburgh (United Kingdom) and IT Center for Science in Espoo (Finland). The

fourth machine is an IBM pSeries 575 at SARA in Amsterdam (the Netherlands). Part of the calculation was done in a ``grid'' computing environment, in which we used more than one machine simultaneously for one run (Portegies Zwart et al. 2010a).

For the time integration we used the GreeM code (Ishiyama et al. 2009b) for single supercomputer runs and the SUSHI code (Groen et al. 2011) for multi-supercomputer runs. The GreeM code is a massively parallel TreePM code based on the parallel TreePM code of Yoshikawa and Fukushige (2005) for large cosmological N-body simulations. The long range forces are calculated by the PM method (Hockney and Eastwood 1981), and the short range forces are calculated by the Barnes-Hut-Tree method (Barnes and Hut 1986). Yoshikawa and Fukushige (2005) used a 1-D slab decomposition, but in GreeM we use a 3-D multi-section decomposition (Makino 2004) to improve its scalability. In addition, the decomposition is based on CPU time measurement, so that near ideal load balance is archived. The SUSHI code is an extension of the GreeM code which can run concurrently on multiple supercomputers. It uses the MPWide communication library (Groen et al. 2010) running on Global Lambda Integrated Facility (GLIF) (DeFanti et al. 2003) to facilitate message passing between distributed supercomputers. We used 512^3 PM grid points for PM calculations, the opening angle for the tree method was 0.3 from initial to $z = 10$, and 0.5 from $z = 10$ to $z = 0$.

The calculation time was $\sim$180s per step with 1024 CPU cores for the largest run on the Cray XT4 in Japan and $\sim$140s per step with 2048 CPU cores on the IBM pSeries 575 in the Netherlands. We spent about 3.5 million CPU hours to perform all the 60,283 steps in our simulation.

We used the spherical overdensity method (Lacey and Cole 1994) to identify haloes and calculated the halo virial radius $R_{\rm vir}$. The virial radius of a halo is defined as the radius in which the spherical overdensity is $\Delta(z)$ times the critical value. The overdensity $\Delta(z)$ is given by the analytic formula (Bryan and Norman 1998),

$$\Delta(z) = (18\pi^2 + 82x - 39x^2)/\Omega(z), \tag{3.1}$$

where $x \equiv \Omega(z) - 1$. The mass of a halo is defined as interior mass within the virial radius.

The mass of the most massive halo is $5.24 \times 10^{13} M_\odot$. It contains 4.08×10^8 particles. Via Lactea I, II (Diemand et al. 2007, 2008), and Aquarius simulations (Springel et al. 2008) used $\sim 10^8$, $\sim 5 \times 10^8$, and $\sim 10^9$ particles for the largest halo. Table 3.2 shows the properties of the three most massive haloes in our simulation.

The subhalo finder is the same as that described in Ishiyama et al. (2009a). Our method is based on the idea of finding all local potential minima. Initially, all

particles are candidates for the centres of haloes. We then search for the particle with the smallest (most negative) potential and regard it as the centre of a halo. We then exclude $n_{\rm min}$ neighbour particles of this particle from the list of remaining particles, and search the particle with the smallest potential from the list. At this time, we again search $n_{\rm min}$ neighbour particles from the list of originally selected particles, and if the potential of one neighbour is smaller, we do not add this particle to the list of haloes. However, we remove $n_{\rm min}$ neighbours no matter whether the particle is added to the list or not. We repeat this procedure until there is no remaining particle. We set $n_{\rm min}$ so that $n_{\rm min} \times m = 1.0 \times 10^7 M_\odot$, where m is the mass of each particle.

Figure 3.1 shows the snapshots at $z = 0$. In Figure 3.2, we also present the time evolution of the whole box and that of the most massive halo. The three most massive haloes in simulations with three different resolutions are shown in Figure 3.3. The positions of subhaloes agree very well in three simulations. Of course, there are some discrepancies near the centres of haloes. In particular, whereas there is only one core in the centre of the second massive halo (GP2) of CG2048, there are two cores in GP2 of CG1024 and CG512.

The reason of this difference is that the formation history of this halo is rather violent. It experienced many mergers near $z = 0$ in the centre of the halo and is far from the relaxed state. The difference of the accuracy of integration changed the time-scale of the mergers of the haloes with three different resolutions. At $z = 0$, the halo GP2 has just completed the merger in the CG2048 run, whereas the same merger event is still on-going in CG1024 and CG512 runs. If we consider the spherically averaged density profile of the halo, the difference becomes important (see Section 3.3.2).

3.3 Results

3.3.1 Mass Function

Press and Schechter (1974) established a recipe to derive the number of dark matter haloes based on the hierarchical clustering model. Since then, a number of analytic formulae for the mass function have been proposed. Many of them are designed to give a good agreement with results of high-resolution N-body simulations (e.g., Sheth and Tormen 1999; Jenkins et al. 2001; Reed et al. 2003; Yahagi et al. 2004; Warren et al. 2006; Tinker et al. 2008, and references therein).

These formulae can reproduce the mass function between $10^{10} M_\odot$ and cluster scale very well. Here, we examine the mass function of mass below $10^{10} M_\odot$ down to $10^7 M_\odot$. The mass function of this range has been studied only in high redshift

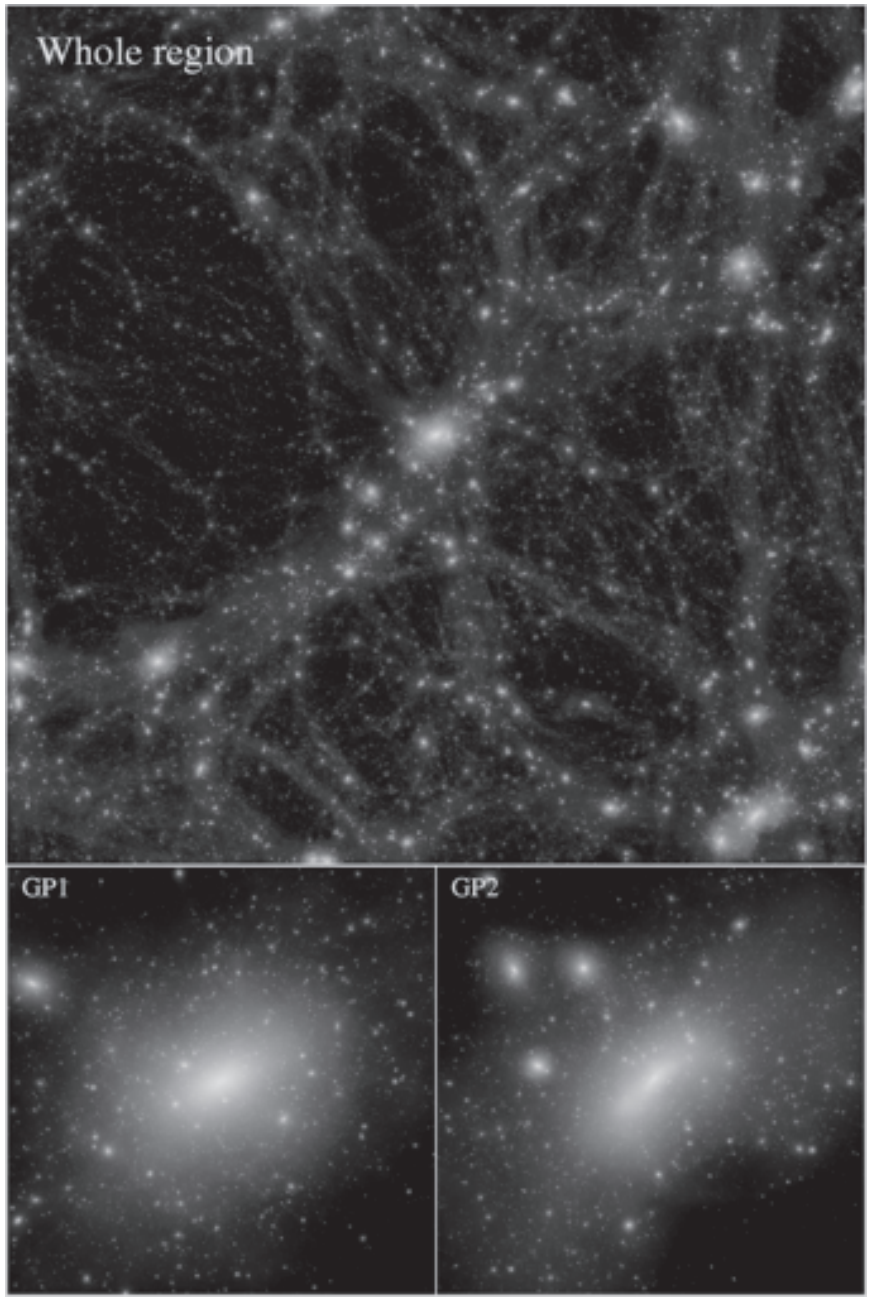

Figure 3.1: Projected density of dark matter at $z = 0$ in our largest simulation (2048^3 particles). Top panel shows the whole region with the volume of $(30\mathrm{Mpc})^3$. Bottom panels show the projected density of the two most massive group sized haloes. These volumes are $(2\mathrm{Mpc})^3$.

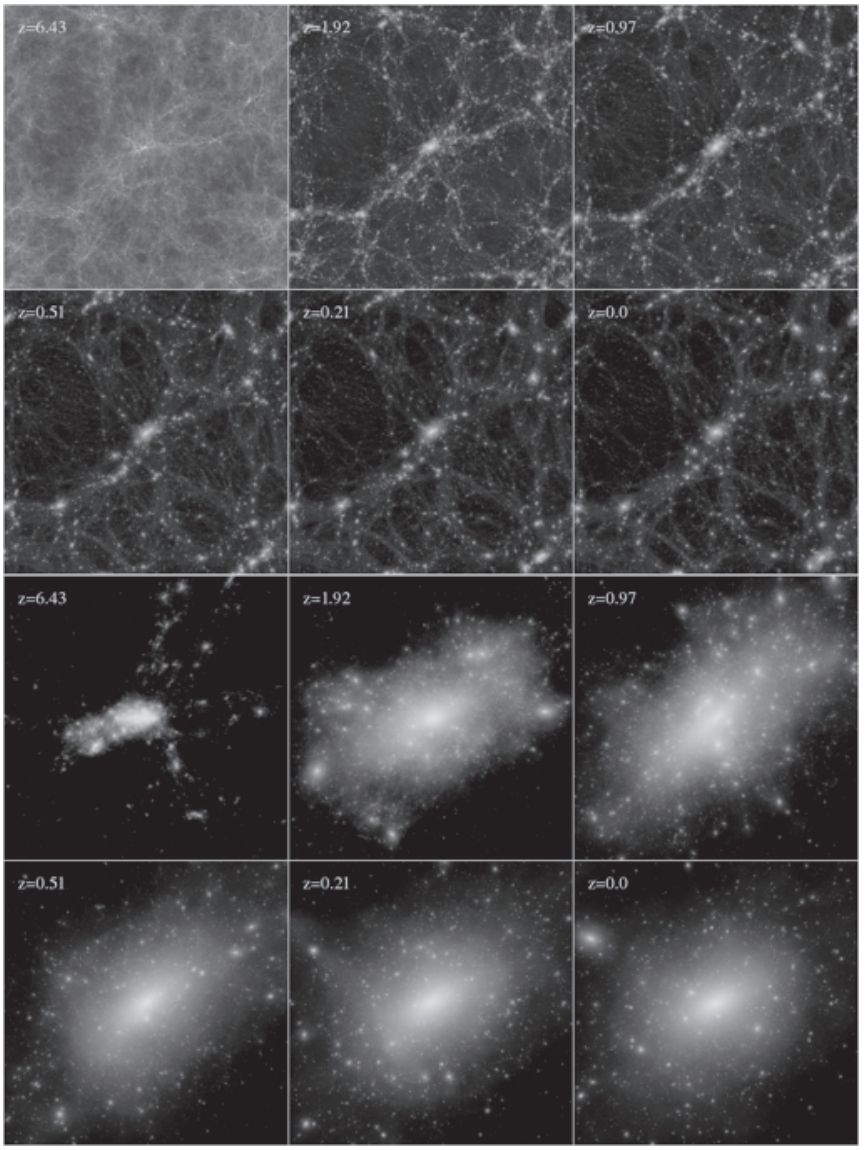

Figure 3.2: Evolution pictures of our largest simulation. Top six panels show the evolution of the whole region. Bottom six panels show the evolution of the most massive halo.

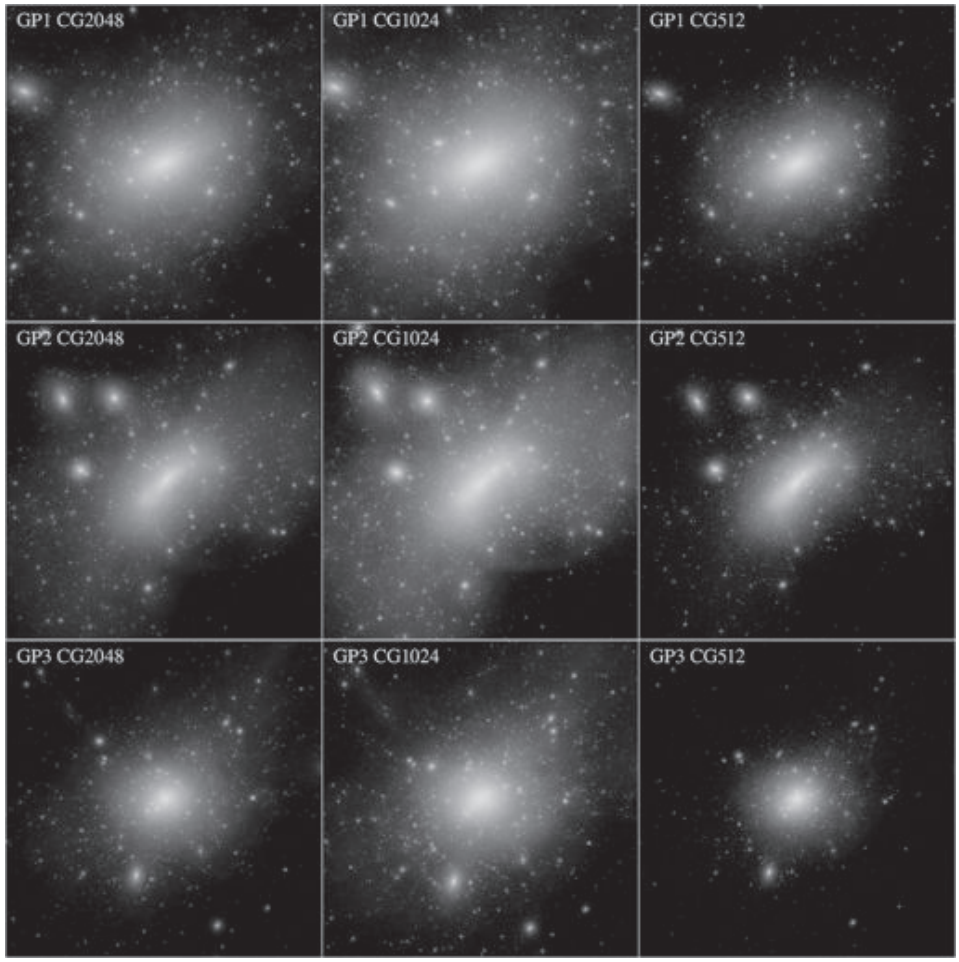

Figure 3.3: Projected density of dark matter at $z = 0$. Each row shows one of the three most massive haloes with mass decreasing from top to bottom. Columns show different resolution from highest (left) to lowest (right).

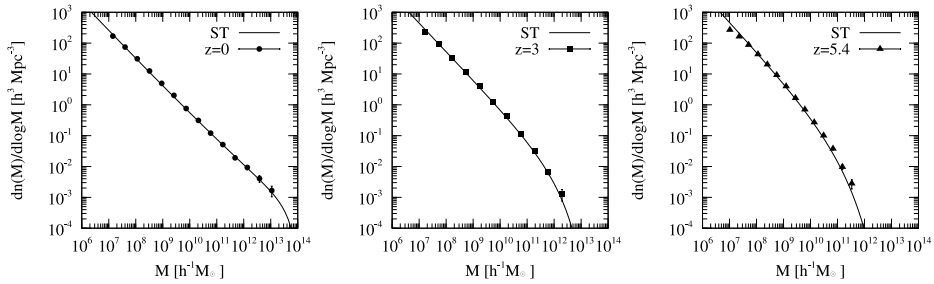

Figure 3.4: Mass function of our largest simulation (CG2048). The results of $z = 0.0$ (left), $z = 3.0$ (middle), and $z = 5.4$ (right) are shown. Solid curves are the Sheth and Tormen (1999) function. Error bars are Poisson errors.

(e.g., Reed et al. 2007; Lukić et al. 2007).

Figure 3.4 shows the halo mass functions at three different redshifts for the CG2048 run and the prediction of Sheth & Tormen formula (ST, Sheth and Tormen 1999). The agreement is very good for the mass from $\sim 10^7 M_\odot$ to $M = 1.0 \times 10^{13} M_\odot$ at $z = 0$. The difference is less than 10% for $M = 5.0 \times 10^7 M_\odot$ to $M = 2.0 \times 10^{12} M_\odot$ at $z = 0$, $M = 5.0 \times 10^7 M_\odot$ to $M = 5.0 \times 10^{10} M_\odot$ at $z = 3$, and $M = 8.0 \times 10^7 M_\odot$ to $M = 4.0 \times 10^9 M_\odot$ at $z = 5.4$.

Our results imply that the mass function is well represented by the ST function down to $10^7 M_\odot$. However, our simulations have a slightly larger number of haloes than the number predicted by the ST formula in particular at the high-mass end of the $z = 5.4$ mass function. Note that the finite volume of our simulation (the box length is 30Mpc) might affect the mass function in some degrees. The absence of long-wavelength perturbations might increase the number of intermediate mass haloes by about 10% (Bagla and Prasad 2006; Power and Knebe 2006). In order to test the effect of the box size, we performed additional simulations of 30, 45, and 60Mpc boxes with 512^3 particles. The left panel of Figure 3.5 shows mass functions of these simulations at $z = 5.4$ relative to the ST formula. The difference becomes larger as the halo mass and the box size increase. The right panel of Figure 3.5 shows mass functions relative to the 30Mpc simulation. We can see that the number of haloes of the 30Mpc box simulation is systematically larger than those of the 45Mpc and 60Mpc box simulations. The mass functions of the 45Mpc and 60Mpc box simulations are well converged for haloes larger than $2.0 \times 10^{10} M_\odot$, which is the limit of resolution for the 60Mpc box simulation. We can conclude that the larger number of haloes seen in CG2048 at the high-mass end is caused by the absence of long-wavelength perturbations.

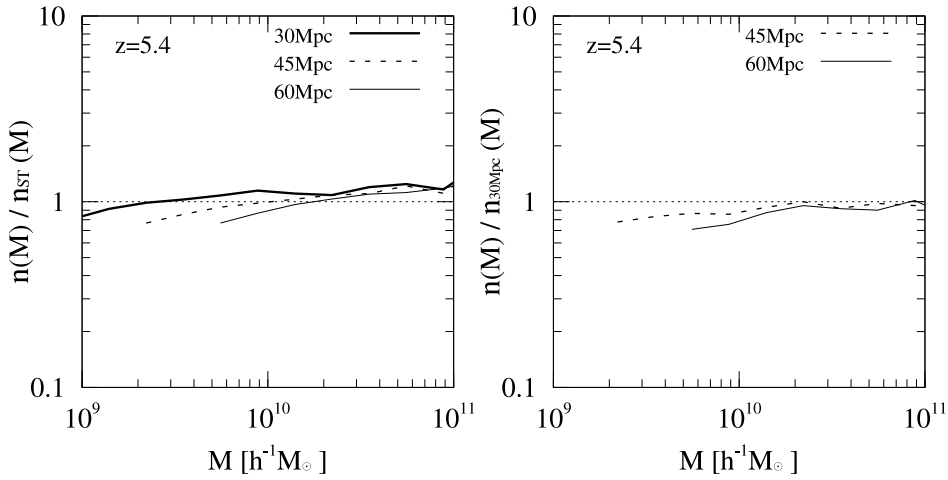

Figure 3.5: Left panel shows three mass functions at $z = 5.4$ derived from 512^3 simulations of 30, 45, and 60 Mpc boxes, relative to the Sheth and Tormen (1999) function. Right panel shows mass functions of 45 and 60 Mpc boxes simulations, relative to that of the 30 Mpc box simulation.

3.3.2 Density Structures of Most Massive Halos

Many groups have studied the density profile of dark matter haloes using high-resolution cosmological N-body simulations (e.g., Navarro et al. 1997; Fukushige and Makino 1997; Moore et al. 1999b; Ghigna et al. 2000; Jing and Suto 2000; Jing 2000; Fukushige and Makino 2001; Klypin et al. 2001; Taylor and Navarro 2001; Jing and Suto 2002; Power et al. 2003; Fukushige and Makino 2003; Fukushige et al. 2004; Diemand et al. 2004; Hayashi et al. 2004; Navarro et al. 2004; Diemand et al. 2005; Reed et al. 2005; Kazantzidis et al. 2006; Merritt et al. 2006; Diemand et al. 2008; Gao et al. 2008; Stadel et al. 2009; Navarro et al. 2010). In most of recent works, the slopes of radial density profiles were around -1 in the inner region and around -3 in the outer region. The slope of density became shallower as the radius becomes smaller. Thus, the central slope is not described by any single power. Furthermore, the density profile was not universal. In other words, the slope showed a significant halo-to-halo scatter.

Recent studies (Stadel et al. 2009; Navarro et al. 2010) based on high-resolution simulations of galactic haloes showed that the slopes of density became less than -1 at the radius 0.001 times the virial radius of the halo as predicted by early works (e.g. Graham et al. 2006). Einasto profile showed better agreement than the NFW profile which has been widely used for modelling dark matter haloes because of its simplicity.

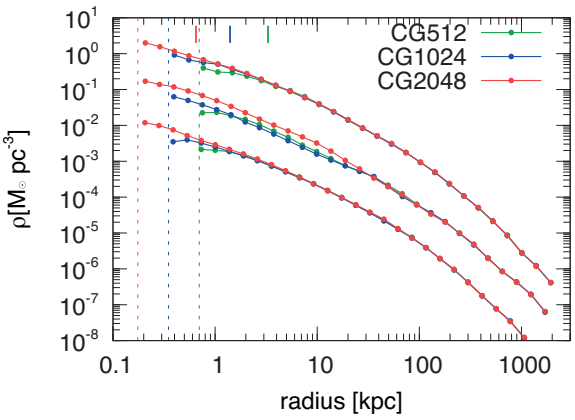

Figure 3.6: Spherically averaged radial density profiles of largest three haloes at $z = 0$. Two of three profiles (middle and bottom) are vertically shifted downward by 1 and 2 dex. Vertical dashed lines show the softening length of three simulations. Upside short vertical bars indicate the reliability limit of the most massive halo calculated using criterion proposed by Fukushige and Makino (2001) and Power et al. (2003). Red, blue, and green correspond to the CG2048, CG1024, and CG512 simulations, respectively.

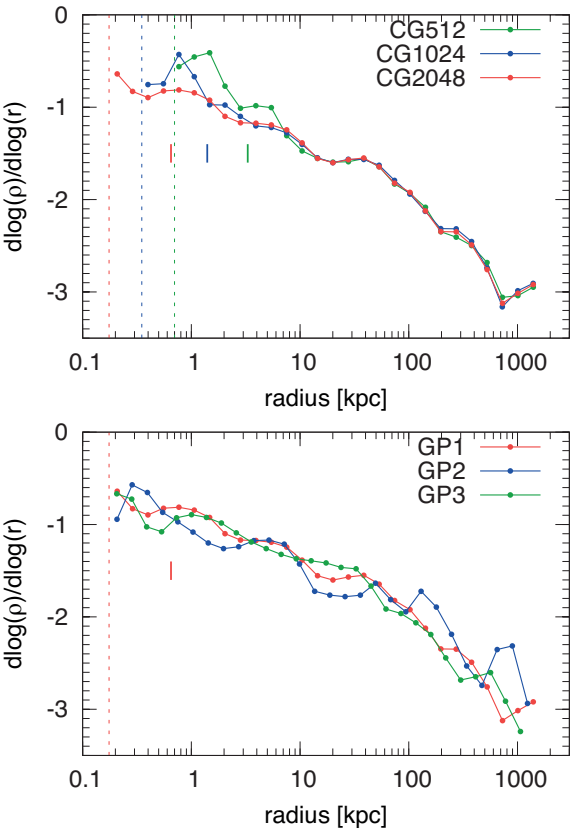

Figure 3.7: Slopes of radial density profiles of largest three haloes at $z = 0$. Top panel shows those of the largest halo for three different resolutions. Bottom panel shows those of the largest three haloes for the largest simulation (CG2048).

Almost all recent high-resolution simulations of single haloes used galaxy-sized haloes. Therefore, little is known if these finding can be applied to haloes of different masses. Here, we present the density profiles of three most massive haloes in our simulation. These haloes are galactic group-sized ones, with the mass of 5.24, 3.58, and 2.25 $\times 10^{13} M_{\odot}$. They contain 408, 279, and 176 million particles.

Figure 3.6 shows the spherically averaged density profiles of these haloes at $z = 0$. We can see that the results of three simulations with different resolution are indistinguishable for radii larger than the reliability limits, except for the second massive halo. We calculated the reliability limits using criterion proposed by Fukushige and Makino (2001) and Power et al. (2003). We cannot ignore the effects of the local two-body relaxation for radii smaller than these limits. As can be seen in Figure 3.3, the slight difference of the merging epoch of the central cores caused this difference.

The slopes of density profiles become gradually shallower as the radius becomes smaller. The top panel of Figure 3.7 shows the slopes of density profiles of the most massive halo. As in the case of the density profile itself, the slopes also agree well with each other. The bottom panel of Figure 3.7 shows the slopes of the three most massive haloes in the CG2048 run.

These profiles are significantly different from those of galactic haloes in recent other high-resolution simulations, even if the halo mass is scaled to be the same. The mass of the haloes of Aquarius simulation (Springel et al. 2008) or GHALO simulation (Stadel et al. 2009) is $\sim 10^{12} M_{\odot}$, which is an order of magnitude smaller than our three haloes. The slope at $0.001 R_{\rm vir}$ is $-0.9 \sim -1.0$ for our three haloes. This value is in excellent agreement with the result of both simulations. Both of them gave the slope -1.0 for $r = 0.001 r_{200}$. This agreement does not mean the density profile obtained by these simulation and those by our simulation are identical. The concentration parameter, which we define here as $c_{\rm vmax} = R_{\rm vir}/R_{\rm vmax}$, is 4.8, where $R_{\rm vir}$ and $R_{\rm vmax}$ are the halo virial radius and the radius of the maximum rotational velocity. This value is significantly smaller than that of Aquarius A-1 halo. Thus, the Aquarius halo is significantly more centrally concentrated, and yet the slope at $r = 0.001 R_{\rm vir}$ is the same. Thus the rate of the shallowing of the slope is somewhat faster for the Aquarius halo than for our CG2048 haloes. Most likely, this difference is due to the difference in the mass of the halo.

3.3.3 Concentration Distributions

The concentration parameter has been widely used to describe the internal structure of haloes since it is tightly correlated with the formation epoch (Wechsler

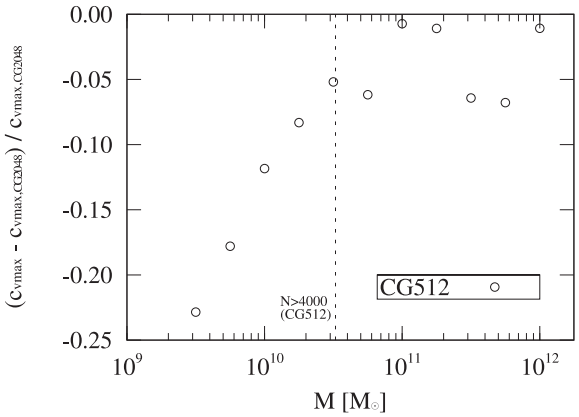

Figure 3.8: Residuals of concentration $c_{\rm vmax} = R_{\rm vir}/R_{\rm vmax}$ from the largest simulation (CG2048) to the lower resolution simulation (CG512).

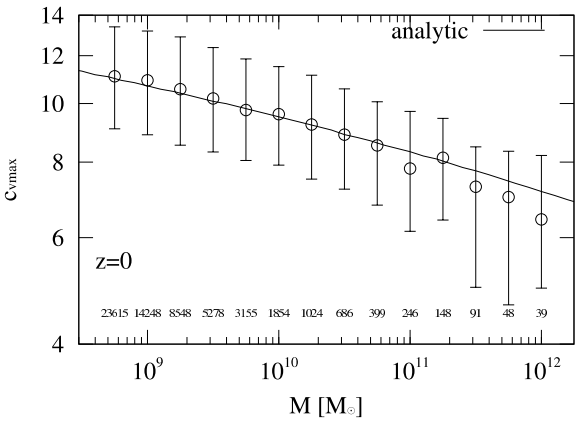

Figure 3.9: Concentration plotted against the halo virial mass M at $z = 0$. Circles show the median value on each bin. Whiskers are the first and third quantiles. The number of haloes on each bin is shown below circles. Thick solid line shows the result from an analytical model.

et al. 2002). Usually, the concentration is parametrised assuming that the density profiles of haloes can be fitted by the NFW profile (Navarro et al. 1997),

$$\rho(r) = \frac{\rho_0}{(r/r_{\rm s})(1 + r/r_{\rm s})^2}, \tag{3.2}$$

where ρ_0 is a characteristic density and r_s is a scale radius. The concentration $c_{\rm NFW} = R/r_s$ is widely used (e.g., Bullock et al. 2001b; Zhao et al. 2003; Macciò et al. 2007; Neto et al. 2007; Macciò et al. 2008; Zhao et al. 2009; Muñoz-Cuartas et al. 2011). It is known that $c_{\rm NFW}$ depends weakly on the halo mass. Halos with higher mass have smaller concentration, since the average density of a halo reflects the cosmic density at its formation time. The dependence is weaker for higher redshift (Zhao et al. 2003).

The concentration based on the NFW profile is affected by fitting ranges and resolution (Neto et al. 2007). Furthermore, recent high-resolution simulations showed that the density profile is significantly different from the NFW profile

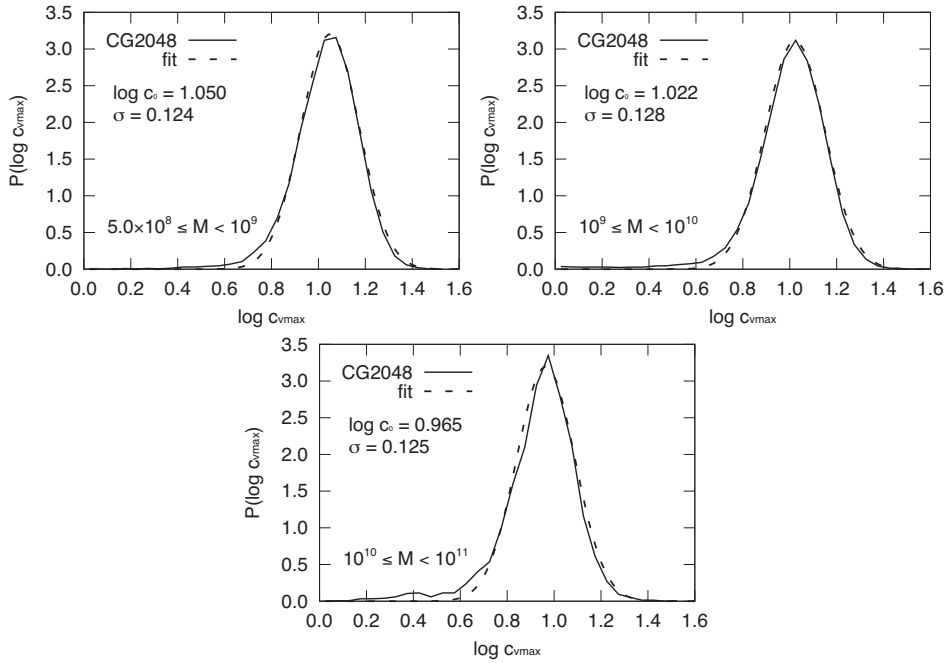

Figure 3.10: The probability distribution functions of the concentration at $z = 0$. These panels show the results of different mass ranges. Dashed curves are the best fits of the log-normal distribution.

(Stadel et al. 2009; Navarro et al. 2010, also see Section 3.3.2). Thus, the use of $c_{\rm nfw}$ might cause some systematic bias (Gao et al. 2008; Reed et al. 2011).

We use the concentration $c_{\rm vmax}$ defined in Section 3.3.2, which is a simpler quantity to measure the concentration. Note that $R_{\rm vmax}$ can be easily determined directly from spherically averaged mass distribution without the need of any fitting formulae. If the density profile is represented by the NFW profile, either concentration can be converted to the other.

First, we determine the minimum number of particles in a halo necessary to reliably determine the concentration. Figure 3.8 shows the normalized difference of average concentration between the G2048 run and the CG512 run as the function of halo mass. We can see that the difference is ~ 0.05 for the halo mass larger than $3.0 \times 10^{10} M_{\odot}$. For halo mass less than $3.0 \times 10^{10} M_{\odot}$, the difference is larger. In the CG512 run, a halo of mass $3.0 \times 10^{10} M_{\odot}$ contains ~ 4000 particles. So we conclude that we need ~ 4000 particles to reliably determine the concentration. For the CG2048 run, the reliability limit is $5.0 \times 10^{8} M_{\odot}$.

Figure 3.9 shows the median, and first and third quantiles of the concentration

as a function of the virial mass of the halo. We can see a clear correlation between the halo mass and the concentration. Apparently, the dependence is weaker for smaller mass. Therefore, the fitting functions with a single power (e.g., Bullock et al. 2001a; Neto et al. 2007; Macciò et al. 2007; Klypin et al. 2011) cannot be used for haloes of the size of dwarf galaxies.

Theoretically, the concentration of a halo reflects the cosmic density at the formation time of the halo (Bullock et al. 2001a). The concentrations of haloes formed earlier are higher than that of haloes formed later. However, the dependence should be weak for small haloes since the dependence of the formation epoch to the halo mass is small for small (smaller than $10^8 M_\odot$) haloes. The slope of the power spectrum of initial density fluctuations approaches to -3 for small mass limit.

In Figure 3.9, we also plot an analytical prediction of the mass--concentration relation, obtained by the method used in Navarro et al. (1997) assuming that all haloes have the NFW profile. The formation redshift $z_{\rm f}$ of haloes with the mass M is defined as the epoch at which progenitors with the mass larger than fM first contained the half of the mass M. It is estimated by using the Press-Schechter formalism (e.g., Lacey and Cole 1993),

$$\mathrm{erfc}\left\{\frac{\delta_{\rm crit}(z_{\rm f})-\delta_{\rm crit}(0)}{\sqrt{2\left[\sigma_0^2(fM)-\sigma_0^2(M)\right]}}\right\}=\frac{1}{2}, \tag{3.3}$$

where $\delta_{\rm crit}(z)$ is the critical overdensity for the spherical collapse at $z_{\rm f}$, and $\sigma_0^2(M)$ is the variance of the density fluctuation at $z=0$ smoothed by a top-hat filter on a mass scale of M. Here, we used $f=0.01$. The characteristic density ρ_0 of a halo should reflect the cosmic density at the formation time. Thus, we assume

$$\rho_0=\rho_{\rm norm}\left(1+z_{\rm f}\right)^3, \tag{3.4}$$

where $\rho_{\rm norm}$ is chosen to fit the simulation results. The mass of a halo with the NFW profile is given by

$$M=4\pi\rho_0 r_{\rm s}^3\left[\ln(1+c)-c/(1+c)\right]. \tag{3.5}$$

The mass and concentration at $z=0$ are related to each other by

$$M=\frac{4}{3}\pi R_{\rm vir}^3\Delta(0)\rho_{\rm crit}=\frac{4}{3}\pi r_{\rm s}^3 c^3\Delta(0)\rho_{\rm crit}, \tag{3.6}$$

where $\rho_{\rm crit}$ is the critical density. From Equations 3.1, 3.3, 3.4, 3.5, and 3.6, we can analytically estimate the concentration of haloes with the mass M.

As mentioned by Lacey and Cole (1993), the estimated formation epoch obtained using Equation 3.3 is not necessarily correct. This is because the formation time defined here corresponds to the epoch at which one of progenitors has a mass larger than fM. This does not mean that the main progenitor has this mass. Nevertheless, as seen in Figure 3.9, the analytical prediction based on Equation 3.3 shows a very good agreement with the result from CG2048 run for haloes with mass smaller than $10^{11}M_{\odot}$. For haloes with the mass larger than $10^{11}M_{\odot}$, the difference between CG2048 results and analytical ones are relatively large. However, these haloes are rare objects in CG2048 run, and the fact might affect the results in some degrees. We can conclude that the shallowing slope of the mass--concentration relation naturally emerges from the nature of the power spectrum of initial density fluctuations.

The slope is slightly shallower than that of $c_{\rm NFW}$ for larger haloes. For the case of $c_{\rm NFW}$, the slope is around -0.10 for relaxed haloes and -0.11 for all haloes (Neto et al. 2007; Macciò et al. 2007). On the other hand, for the CG2048 simulation, the slope is around -0.07 for haloes with the mass $10^{10}M_{\odot}$, and -0.06 for haloes with the mass $10^{9}M_{\odot}$. Note that one overestimates the central density of haloes if one estimates the concentration of dwarf-sized haloes by extrapolating the mass--concentration relation of galaxy or cluster-sized haloes.

Figure 3.10 shows the probability distribution functions of the concentration parameter at $z = 0$ in three different mass ranges. Both shapes are well fitted by the log-normal distributions,

$$P(\log c_{\rm vmax}) = \frac{1}{\sqrt{2\pi}\sigma} \exp\left(-\frac{\log^2\left(c_{\rm vmax}/c_0\right)}{2\sigma^2}\right). \tag{3.7}$$

We find $\log c_0 = 1.050, \sigma = 0.124$ for haloes with the mass of $5.0\times10^8 M_{\odot} \leqslant M < 10^9 M_{\odot}$, $\log c_0 = 1.022, \sigma = 0.128$ for haloes with the mass of $10^9 M_{\odot} \leqslant M < 10^{10} M_{\odot}$, and $\log c_0 = 0.965, \sigma = 0.125$ for haloes with the mass of $10^{10} M_{\odot} \leqslant M < 10^{11} M_{\odot}$.

3.3.4 Spin Distributions

The dimensionless spin parameter is a good parameter to quantify the rotation of a halo. One often uses the spin parameter defined in Bullock et al. (2001a),

$$\lambda = \frac{J}{\sqrt{2}MVR}, \tag{3.8}$$

where M, R, V, and J are the virial mass of the halo, radius, rotational velocity at R, and total angular momentum inside R.

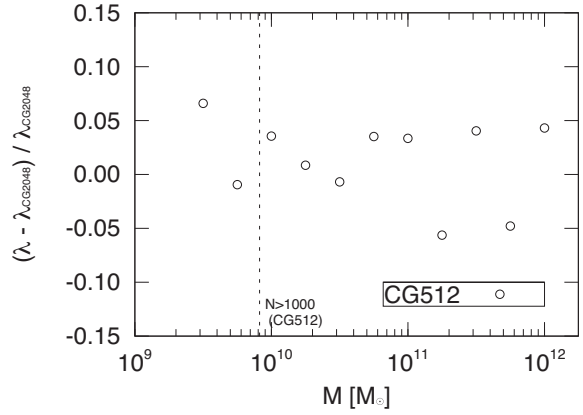

Figure 3.11: Residuals of spin from the largest simulation (CG2048) to lower resolution simulation (CG512).

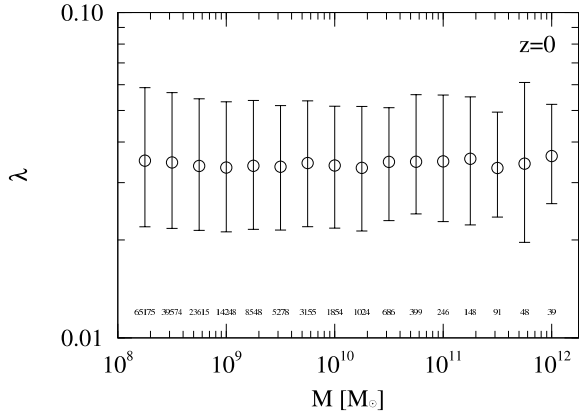

Figure 3.12: Spin parameter λ plotted against the halo virial mass M at $z = 0$. Circles show the median value on each bin. Whiskers are the first and third quantiles. The number of haloes on each bin is shown below circles.

The distribution, the dependence on the halo mass, and the evolution have been studied by a number of works (e.g., Bullock et al. 2001a; Bailin and Steinmetz 2005; Bett et al. 2007; Macciò et al. 2007; Knebe and Power 2008; Macciò et al. 2008; Antonuccio-Delogu et al. 2010; Muñoz-Cuartas et al. 2011; Wang et al. 2011). The spin of galaxy-sized haloes is well studied by using the results of sufficient resolution simulations. However, we do not understand those of dwarf-galaxy-sized haloes. The spin distribution of those haloes at only high redshifts is studied by the result of high-resolution simulation (Knebe and Power 2008). Here, we extend the spin distributions at $z = 0$ to dwarf-galaxy-sized haloes (down to $10^8 M_\odot$) in the same way as the concentration.

First, we determine the minimum number of particles in a halo necessary to reliably determine the spin as done for the concentration. Figure 3.11 shows the normalized difference of average spin between the CG2048 run and the CG512 run as a function of halo mass. We can see that the difference is ~ 0.05 for halo

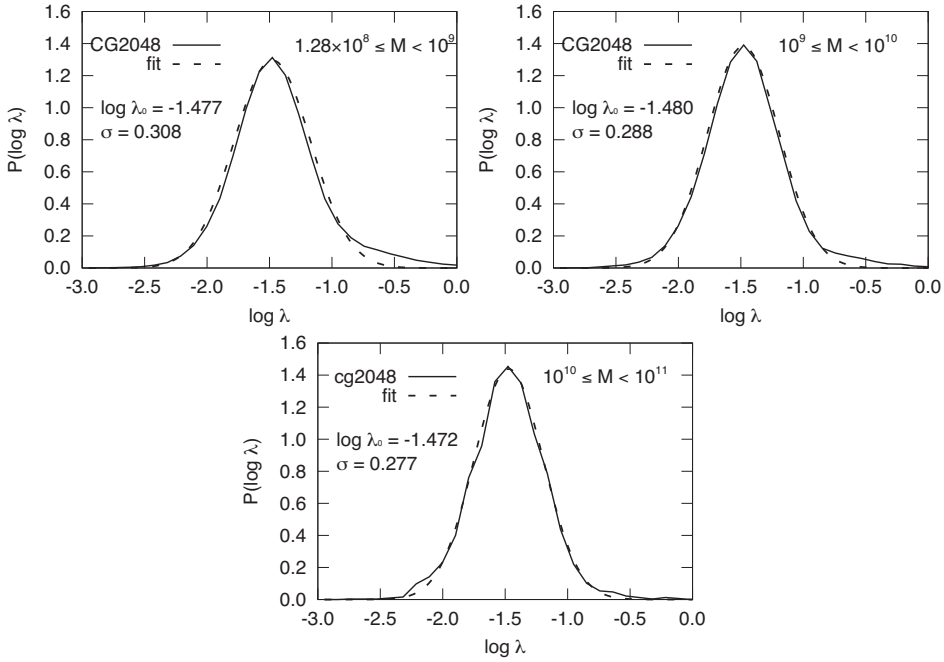

Figure 3.13: Probability distribution functions of the spin parameter at $z = 0$. These panels show the results of different mass ranges. Dashed curves are the best fits of the log-normal distribution.

mass larger than $8.0\times10^9 M_\odot$. For halo mass less than $8.0\times10^9 M_\odot$, the difference is large.

In the CG512 run, a halo of mass $8.0\times10^9 M_\odot$ contains ~ 1000 particles. So we conclude that we need ~ 1000 particles to reliably determine the concentration. For the CG2048 run, the reliability limit is $1.28\times10^8 M_\odot$.

Figure 3.12 shows the median, and first third quantiles of the spin parameter as a function of the virial mass of the halo. Apparently, we can see the spin parameter is independent of the mass down to $10^8 M_\odot$ as pointed out for larger haloes in previous works (Macciò et al. 2007; Muñoz-Cuartas et al. 2011). The median value is 0.0336.

Figure 3.13 shows the probability distribution functions of the spin parameter at $z = 0$ in three different mass ranges. The distributions are well fitted by the log-normal distributions,

$$P(\log\lambda) = \frac{1}{\sqrt{2\pi}\sigma}\exp\left(-\frac{\log^2(\lambda/\lambda_0)}{2\sigma^2}\right). \tag{3.9}$$

We find $\log\lambda_0 = -1.477, \sigma = 0.308$ for haloes with the mass of $1.28\times10^8 M_\odot \leqslant M < 10^9 M_\odot$, $\log\lambda_0 = -1.480, \sigma = 0.288$ for haloes with the mass of $10^9 M_\odot \leqslant M < 10^{10} M_\odot$, and $\log\lambda_0 = -1.472, \sigma = 0.277$ for haloes with the mass of $10^{10} M_\odot \leqslant M < 10^{11} M_\odot$. Thus, we conclude that there is no mass dependence of the spin parameter. Otherwise, it is extremely weak.

We can see that there are small deviations from the log-normal distributions at high spin regions as seen in previous works for larger haloes (Bett et al. 2007; Antonuccio-Delogu et al. 2010). We will discuss the effect of the dynamical state of haloes in Appendix 3.A.

3.3.5 Subhalo

The statistics of the subhalo abundance of galaxy-sized haloes have been well studied (e.g., Ishiyama et al. 2009a; Boylan-Kolchin et al. 2010; Busha et al. 2011). The subhalo abundance shows large halo-to-halo variations and depends on the concentration parameter. Halos with larger concentrations have a smaller number of subhaloes. This means that the number of subhaloes should increase as the halo mass increases since the concentration decreases. However, little is known on how the subhalo abundance depends on the halo mass. The reason is that we need a number of well-resolved haloes in a wide mass range to determine the mass dependence and it is computationally expensive to perform simulations for this purpose.

Contini et al. (2012) analysed the fraction of halo mass in subhaloes for group-sized to cluster-sized haloes and showed that the fraction increases with increasing

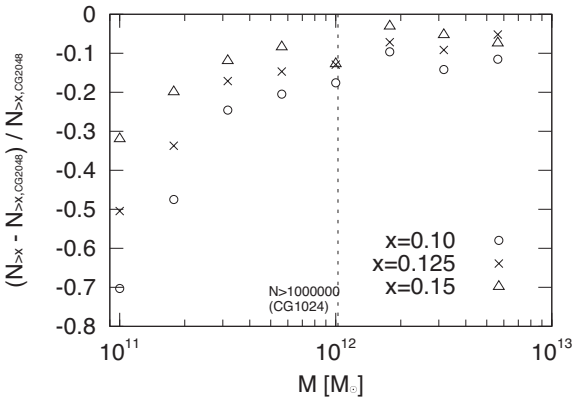

Figure 3.14: Residuals of the subhalo abundance from the largest simulation (CG2048) to lower resolution simulation (CG1024). Here, $N_{>x}$ is the number of subhaloes with rotation velocity larger than x of that of the parent halo.

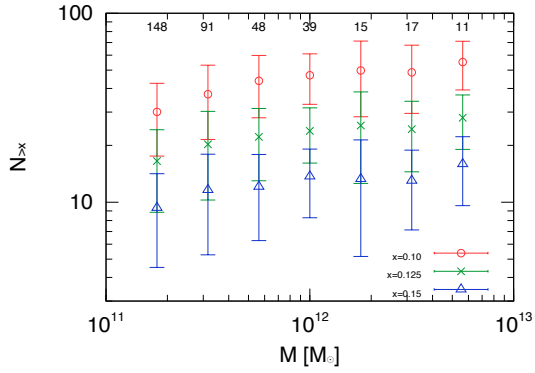

Figure 3.15: Number of subhaloes plotted against the halo virial mass M at $z = 0$. Each symbol shows the mean value on each bin. Whiskers are the standard deviation. The number of haloes on each bin is shown above.

mass. For group-sized haloes, it is approximately 5%, and for cluster-sized haloes approximately 10% (similar results are obtained in Gao et al. 2011, for a slightly different mass range). However, the number of particles per halo of their group-sized haloes is 10^5, which is insufficient to robustly estimate the subhalo abundance (see also Ishiyama et al. 2009a). Therefore, it is possible that they have underestimated the subhalo abundance.

Our high-resolution simulations are suitable for the study of the statistics of the subhalo abundance for haloes with smaller mass. Therefore we can address a key question, how the subhalo abundance depends on the halo mass. Hereafter, we define $N_{>x}$ as the subhalo abundance, which is the number of subhaloes with rotation velocity larger than x times that of the parent halo. Figure 3.14 shows the normalized difference of average subhalo abundance between the CG2048 run and the CG1024 run as a function of halo mass for $x = 0.10, 0.125, 0.15$. We can see that both results are well converged for haloes with more than one million particles for all values of x. For haloes with less particles, the difference becomes larger as the halo mass decreases. Thus, we can conclude that we need about one million particles to reliably determine the subhalo abundance. For the CG2048 run, the reliability limit is $1.28 \times 10^{11} M_\odot$ for $x = 0.1$.

The reliability limit should be smaller for larger subhaloes (larger values of x) since they consist of more particles than smaller ones. As seen in Figure 3.14, the residual of the subhalo abundance is systematically smaller for larger subhaloes (larger x). However, for simplicity, we use the same reliability limit for all values of x. Thus, our choice of the reliability limit is quite conservative.

Figure 3.15 shows the mean and the standard deviation of the subhalo abundance as a function of the virial mass of the halo. We can see clearly that the subhalo abundance depends on the halo mass for all values of x. The average number of subhaloes $N_{>0.10}, N_{>0.125}, N_{>0.15}$ are 30.1, 16.5, 9.3 for haloes with the mass of $\sim 2 \times 10^{11} M_\odot$ and 47.0, 23.8, 13.7 for haloes with the mass of $\sim 1 \times 10^{12} M_\odot$. For haloes with the mass of larger than $\sim 1 \times 10^{12} M_\odot$, we can see that the dependence becomes weaker and gradually approaches to a constant value.

This trend has not been observed in previous works (Gao et al. 2011; Contini et al. 2012), since they analysed haloes with larger mass. However, our result is limited by the box size of the simulation. Since the number of subhaloes with the mass larger than $1 \times 10^{12} M_\odot$ in our simulation is only 82, our haloes within this mass range might be a biased sample. In order to clarify the dependency, larger box simulations are needed.

3.4 Discussions and Summary

We present the first scientific results of the CosmoGrid simulation. Because of unprecedentedly high-resolution and powerful statistics, the simulation is suitable to resolve internal properties of haloes with the mass larger than dwarf galaxy and subhaloes whose scales are comparable to ultra-faint dwarf galaxies.

We summarize the main results of this paper as follows.

- The halo mass function is well described by the Sheth and Tormen (1999) fitting function down to $\sim 10^7 M_\odot$ from $1.0 \times 10^{13} M_\odot$. The differences are less than 10% at $z = 0$ from $M = 5.0 \times 10^7 M_\odot$ to $M = 2.0 \times 10^{12} M_\odot$.

- We analysed the spherically averaged density profiles of the three most massive haloes which contain more than 170 million particles. Their masses are 5.24, 3.58, and 2.25 $\times 10^{13} M_\odot$. We confirmed that the slopes of density profiles of these haloes become shallower than -1 at the inner most radius. The results are consistent with the recent studies based on high-resolution simulations for galactic haloes.

- We studied internal properties of haloes at $z = 0$ with the mass more than $\sim 10^8 M_\odot$. The concentration parameter measured by the maximum rotational velocity radius is weakly correlated with the halo mass. We found that the dependence of the concentration parameter with halo mass cannot be expressed by a single power law, but levels off at small mass. The slope of the mass--concentration relation is around -0.07 for haloes with the mass $10^{10} M_\odot$, and -0.06 for haloes with the mass $10^9 M_\odot$. The shallowing slope naturally emerges from the nature of the power spectrum of initial density fluctuations. A simple model based on the Press-Schechter theory gives reasonable agreement with the simulation result. The spin parameter does not show a correlation with the halo mass. The probability distribution functions of concentration and spin are well fitted by the log-normal distribution for haloes with the mass larger than $\sim 10^8 M_\odot$.

- The subhalo abundance depends on the halo mass. Galaxy-sized haloes have 50% more subhaloes than $\sim 10^{11} M_\odot$ haloes have. We find a new result that the dependence becomes weaker for more massive haloes.

Acknowledgements

We thank the anonymous referee for his/her valuable comments. Numerical computations were partially carried out on Cray XT4 at Center for Computational Astrophysics, CfCA, of National Astronomical Ob-

servatory of Japan, the K computer at the RIKEN Advanced Institute for Computational Science (Proposal number hp120286), Huygens at the Dutch National High Performance Computing and e-Science Support Center, SARA (Netherlands), HECToR at the Edinburgh Parallel Computing Center (United Kingdom), and Louhi at IT Center for Science in Espoo (Finland).

T.I. is financially supported by Research Fellowship of the Japan Society for the Promotion of Science (JSPS) for Young Scientists. This research is partially supported by the Special Coordination Fund for Promoting Science and Technology (GRAPE-DR project), Ministry of Education, Culture, Sports, Science and Technology, Japan.

We also thank the network facilities of SURFnet, DEISA, IEEAF, WIDE, Northwest Gigapop and the Global Lambda Integrated Facility (GLIF), NSF funded TransLight project, National LambdaRail, StarLight, NetherLight, T-LEX, Pacific and Atlantic Wave.

This research is supported by the Netherlands organization for Scientific research (NWO) grants #639.073.803, #643.200.503 and #643.000.803, the Stichting Nationale Computerfaciliteiten (project ♯SH-095-08), NAOJ, SURFnet (GigaPort project), the International Information Science Foundation (IISF), the Netherlands Advanced School for Astronomy (NOVA), the Leids Kerkhoven-Bosscha fonds (LKBF). We thank the DEISA Consortium (EU FP6 project RI-031513 and FP7 project RI-222919) for support within the DEISA Extreme Computing Initiative (GBBP project). This work has been funded by MEXT HPCI STRATEGIC PROGRAM and MEXT/JSPS KAKENHI Grand Number 24740115.

3.A The Effect of Dynamical State of Halos

There are large variations in the dynamical state of haloes. Halos which formed in an early epoch tend to be dynamically relaxed, whereas haloes which experienced a recent major merger tend to be dynamically unrelaxed. The relaxation state of haloes might have some effect on properties of haloes such as the concentration and the spin. Here, we analyse these properties for only dynamically relaxed sample of haloes and discuss the effect of the relaxation state.

Power et al. (2012) argued that the centre-of-mass offset is a robust estimator of the relaxation state of haloes. The centre-of-mass offset is defined as

$$\Delta r = \frac{|\boldsymbol{r}_{\rm cen} - \boldsymbol{r}_{\rm cm}|}{R_{\rm vir}}, \tag{3.10}$$

where $\boldsymbol{r}_{\rm cen}$, $\boldsymbol{r}_{\rm cm}$, and $R_{\rm vir}$ are the centre of density, mass, and the virial radius of a halo. They found that $\Delta r \leqslant 0.04$ is a sufficient condition to pick up dynamically relaxed haloes at $z = 0$. We use this condition to construct the relaxed sample of haloes from our all halo samples.

Figure 3.16 shows the average centre-of-mass offset and the fraction of relaxed haloes as a function of the halo virial mass. The offset increases with increasing the halo mass. This trend is in good agreement with the results of Power et al. (2012).

It is simply because lower mass haloes tend to form earlier than higher mass haloes from the nature of the hierarchical structure formation. As a result, the fraction of relaxed haloes becomes large for lower mass haloes. We can see the offset increases with decreasing the halo mass from $\sim 5 \times 10^8 M_\odot$. This may be caused by the resolution effect.

One may wonder whether the dependence of concentrations to the halo mass is caused by unrelaxed haloes or not. Figure 3.17 shows the median concentration and spin for all and the relaxed sample of haloes as a function of the virial mass of the halo. The relaxation state has little impact on the concentration for haloes smaller than $10^{11} M_\odot$. This can be interpreted as the fact that the fraction of relaxed haloes is large for lower mass haloes as we can see in Figure 3.16.

The spin parameters of relaxed haloes are systematically smaller than those of all haloes by $\sim 8 - 10\%$ for all mass ranges. This result is consistent with early studies (Macciò et al. 2007, 2008). This is because unrelaxed haloes tend to experience a recent major merger, giving them higher spin values. Figure 3.18 shows the probability distribution functions of the spin parameter at $z = 0$ in three different mass ranges. We can see clearly that the number of haloes with high spin values in the relaxed sample of haloes is smaller than that in all sample of haloes for all mass ranges. We find $\log \lambda_0 = -1.514, \sigma = 0.286$ for haloes with the mass of $1.28 \times 10^8 M_\odot \leqslant M < 10^9 M_\odot$, $\log \lambda_0 = -1.520, \sigma = 0.265$ for haloes with the mass of $10^9 M_\odot \leqslant M < 10^{10} M_\odot$, and $\log \lambda_0 = -1.519, \sigma = 0.265$ for haloes with the mass of $10^{10} M_\odot \leqslant M < 10^{11} M_\odot$. The standard deviations are also systematically smaller for relaxed haloes by $\sim 4 - 8\%$.

Small deviations from the log-normal distributions at high spin regions for all haloes are also seen for relaxed haloes. The deviations become weaker since unrelaxed haloes with higher spin are removed.

It is interesting that the spin is relatively influenced by the relaxation state more than the concentration. This might be because haloes grow in a self-similar way (e.g., Fukushige and Makino 2001). The self-similar growth means that the inner region of a halo forms earlier than the outer region. Here, the spin is calculated using all particles. The concentration is estimated using particles within the radius of the maximum rotational velocity, which should be more dynamically relaxed than particles in outer region. Therefore, it is natural that the effect of the relaxation state on the concentration and spin shows such difference.

In summary, we find that the relaxation state makes small difference on the concentration and spin distributions.

- The impact of the relaxation state on the concentration is negligible for haloes smaller than $10^{11} M_\odot$.

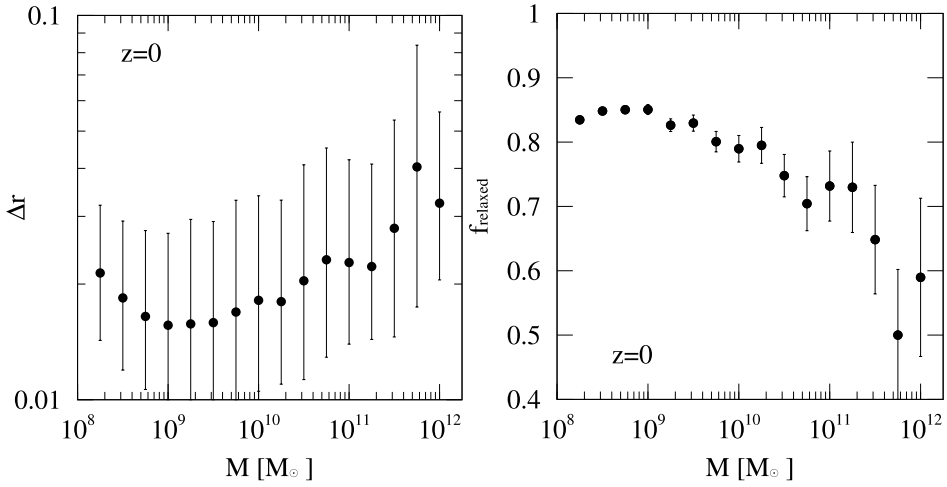

Figure 3.16: Left: the centre-of-mass offset of all haloes plotted against the halo virial mass M at $z = 0$. The median value of each bin is shown by circles. Whiskers are the first and third quantiles. Right: the fraction of relaxed haloes. Error bars are Poisson errors.

- The spin parameters of relaxed haloes are systematically smaller than those of all haloes by $\sim 8-10\%$ for all mass ranges. The spin distributions of relaxed haloes deviate from the log-normal fitting less than those of all haloes.

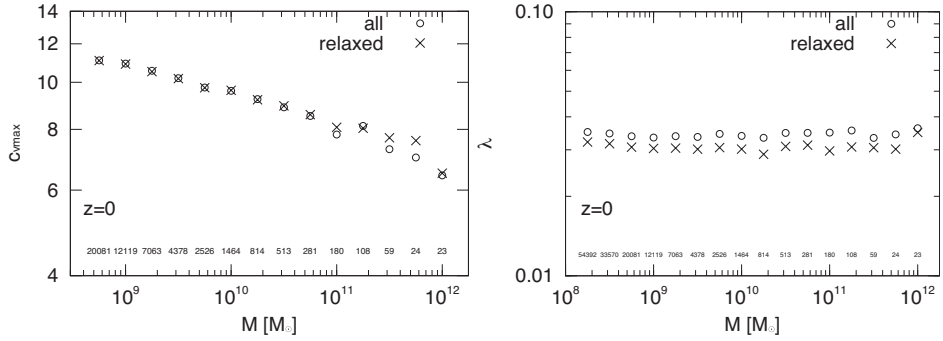

Figure 3.17: Concentration (left) and spin (right) plotted against the halo virial mass M at $z = 0$. The median values of all haloes are shown by circles. Crosses are for the values of only relaxed haloes. The number of relaxed haloes on each bin is shown below.

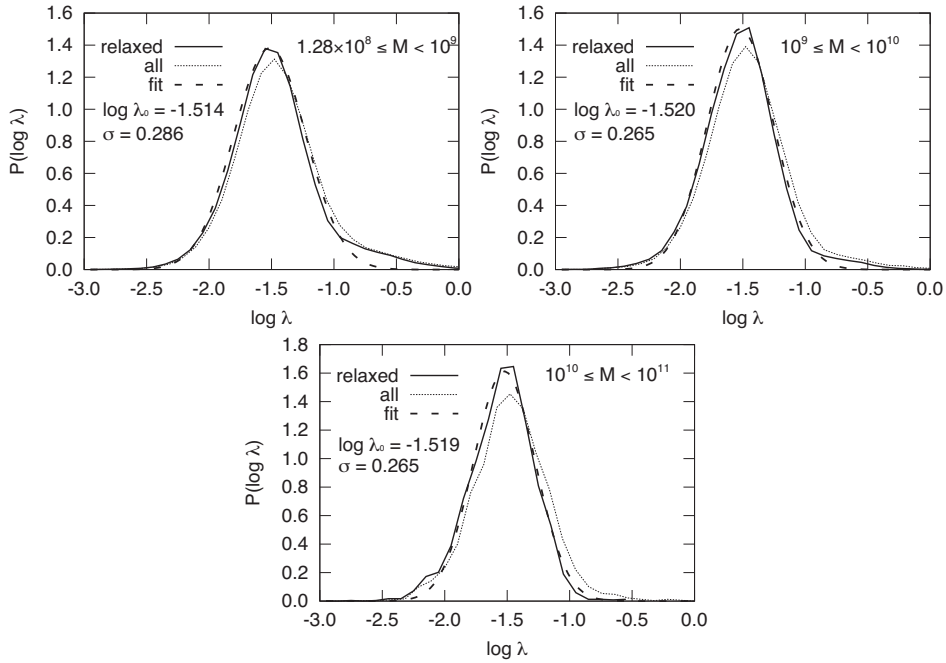

Figure 3.18: Probability distribution functions of the spin parameter at $z = 0$ for relaxed haloes (solid) and all haloes (dotted). Dashed curves are the best fits of the log-normal distribution for relaxed haloes.